Modelling and scaling procedure of a vehicle electric drive system

Modelling and scaling procedure of a vehicle electric drive system

Emma Arfa Grunditz and Torbjörn Thiringer

Department of Electrical Engineering
CHALMERS UNIVERSITY OF TECHNOLOGY
Göteborg, Sweden 2017

Modelling and scaling procedure of a vehicle electric drive system

Emma Arfa Grunditz and Torbjörn Thiringer

Department of Electrical Engineering
CHALMERS UNIVERSITY OF TECHNOLOGY
Göteborg, Sweden 2017

Modelling and scaling procedure of a vehicle electric drive system

Technical report 2017:1

Department of Electrical Engineering

Division of Electric Power Engineering

Chalmers University of Technology

SE-412 96 Göteborg

Sweden

Modelling and scaling procedure of a vehicle electric drive system

Abstract

This report describes the modelling and scaling of the drive systems in a small and a large BEV. Typical drive system components (electric motor, inverter, battery and transmission) are chosen, and modeled. Initially all components are sized in order for the two BEVs to fulfill a set of specified vehicle requirements. Then the electric motor is scaled by axial length in order to give a linearly varying output power and torque. A scalable inverter model is suggested that scales with the current rating, for a fixed voltage rating.

I. Initial Reference System Sizing Based on Vehicle Parameters and Requirements

For the analysis in this report two highway capable light duty BEVs, a Small and a Large, have been conceptualized based on dimensional and performance data from numerous available passenger BEVs on the market [1]. The concept BEV's parameters and requirements, shown in Table I, are aimed to represent an average small and large BEV, rather than specific models. Furthermore, the Small BEV is to be designed for urban driving with moderate speed levels, and the Large BEV for a large portion of rural driving at higher speed levels.

TABLE I
VEHICLE PARAMETERS AND PERFORMANCE REQUIREMENTS, FOR THE REFERENCE SYSTEMS.

	Small BEV	**Large BEV**
Curb weight	1200 kg	1708 kg
Aerod. drag coeff. C_d:	0.31	0.29
Front area:	2.1 m^2	2.3 m^2
Wheel radius:	0.30 m	0.32 m
Rolling resist. coeff. C_r:	0.007	0.007
Top speed:	130 km/h	145 km/h
Acceleration 0-100 km/h:	13 s	10 s
Starting gradability:	25 %	25 %
Gradability: (Speed at grade)	90 km/h at 6%	130 km/h at 6%
NEDC Range:	160 km	200 km
Gear ratio:	10.440	9.984

The drive system in each of the two BEVs consists of a battery, inverter, electric motor and a fixed speed transmission as in Fig. 1. The initial sizing however only considers the forces on the wheel shaft.

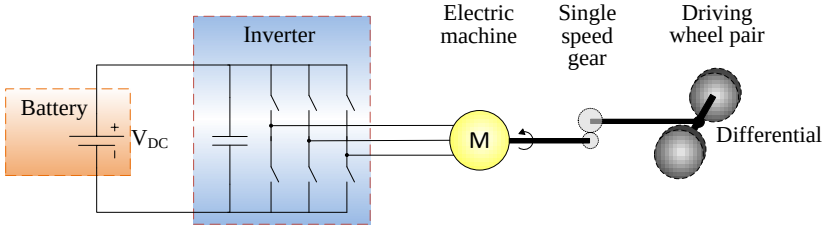

Fig. 1. The BEV drive system.

Similarly as in [2]–[4], the force, speed and power on the wheel shaft that has to come from the drive system in order to sustain the requirements are determined using vehicle dynamic equations. Then the vehicle's instantaneous wheel force F_{wheel} is the sum of the aerodynamic force, the rolling resistance, the acceleration force and the road grade force as

$$F_{wheel} = \frac{\rho}{2} C_d A v^2 + C_r m g cos\alpha + m g sin\alpha + m\frac{dv}{dt} \quad (1)$$

where ρ is the air density ($1.2\,kg/m^3$), $v\,(m/s)$ the longitudinal vehicle speed, $m\,(kg)$ the total rolling mass, g the gravitational constant ($9.81\,m/s^2$) and $\alpha\,(rad)$ the road gradient [5]. For simplicity, only longitudinal vehicle motions are considered. Moreover, the term *road load* refers in this paper to the wheel force due to the sum of rolling resistance and aerodynamic drag. Furthermore, the instantaneous wheel power, P_{wheel}, is the product of the wheel force and vehicle speed ($P_{wheel} = v\,F_{wheel}$).

The results regarding starting gradability and road load on level and non-level road as a function of speed are presented in Fig. 2. The largest power levels of 26 kW for the Small BEV and 59 kW for the Large, are both reached during high speed driving with 6% road grade. The starting gradeability demands an initial wheel force of 2937 N and 4161 N for the Small and Large BEV respectively.

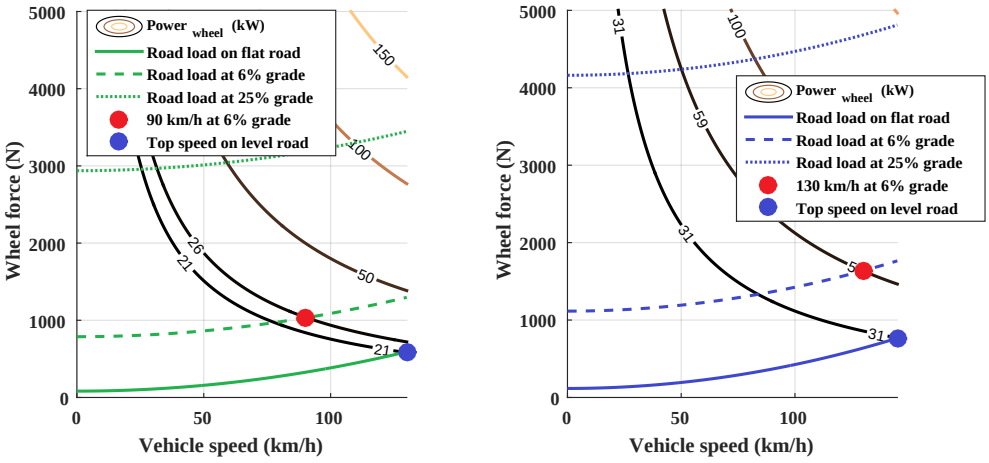

(a) Small car. (b) Large car.

Fig. 2. Force on wheels for level and non-level road load, along with wheel power contour lines. Also, the top speed and high speed gradeability requirements are especially marked.

As shown in [4] with a fixed max speed, the 0-100 km/h acceleration time requirement can be fulfilled by more than one value of the base speed when the max torque and power are allowed to vary as well. This is valid under the assumption of an ideal electric motor output with a max torque that is constant up to base speed and then decays with increasing speed since in this case the power is constant for increasing speed.

Here, three combinations of max force and power are identified for each BEV, at the base-to-top speed ratios of 1/4, 1/3 and 1/2 as shown in Fig. 3a and Fig. 3b. The aerodynamic drag and rolling resistance are included in the calculations. The chosen base-to-top speed ratios reflect noted values for motors in available electric vehicles [1].

In order to prioritize low speed acceleration performance for the Small BEV the base-to-top speed ratio of 1/4 is chosen. This gives an expected acceleration time 0-50 km/h of 3.9 s and an initial max wheel force of **5 kN**, and a max power of **44.7 kW**. As the Large car on the other hand should be designed to perform well also at higher speed levels, the base-to-top speed ratio of 1/3 is chosen. Then the expected acceleration time 0-50 km/h is 3.8 s. The initial max wheel force is **6.5 kN**, and the max power is **86.6 kW**.

To conclude, the single requirement that demands the largest force and power from the drive system to the wheels is the acceleration requirement.

II. General Component Sizing Procedure

The aim is to use drive system component models which represent typical characteristics for this type of application. Therefore, based on findings in [1], [6], the drive system consists of a permanent magnet synchronous motor (PMSM), a fixed transmission ratio, an IGBT (insulated-gate bipolar transistor) inverter, and a lithium ion battery.

A methodology for the general design procedure of the BEV components that is used here, is presented in Fig 4 and is further described in the following sections.

The wheel force relates to the electric machine torque T_{EM} and speed n_{EM} via the wheel radius r, the transmission gear ratio k_{gear} and transmission efficiency η_{gear}, in motoring mode as

$$T_{EM} = \frac{r\, F_{wheel,PT}}{\eta_{gear}\, k_{gear}} \tag{2}$$

and

$$n_{EM} = k_{gear} \frac{v}{r} \frac{60}{2\pi} = k_{gear} w_{wheel} \frac{60}{2\pi} \tag{3}$$

where the wheel rotational speed w_{wheel} (rad/s) is the ratio of vehicle speed and wheel radius [5].

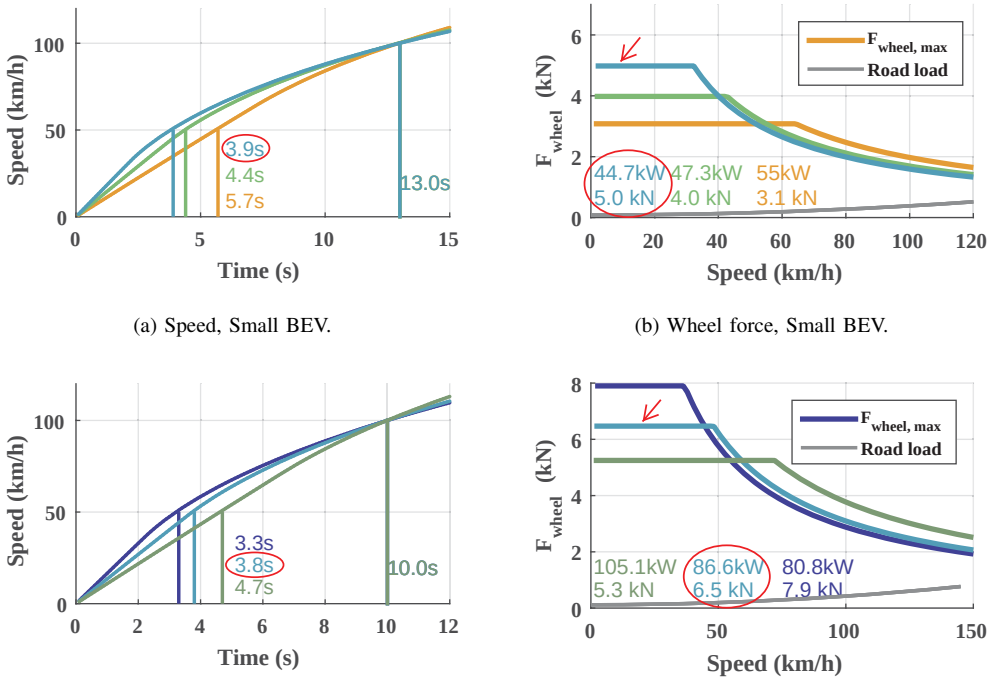

(a) Speed, Small BEV.

(b) Wheel force, Small BEV.

(c) Speed, Large BEV.

(d) Wheel force, Large BEV.

Fig. 3. Speed over time, as well as wheel force over speed, for base speeds that are $1/4$, $1/3$ and $1/2$ of the top speed, during $0-100\,km/h$ acceleration, for the Small and Large car.

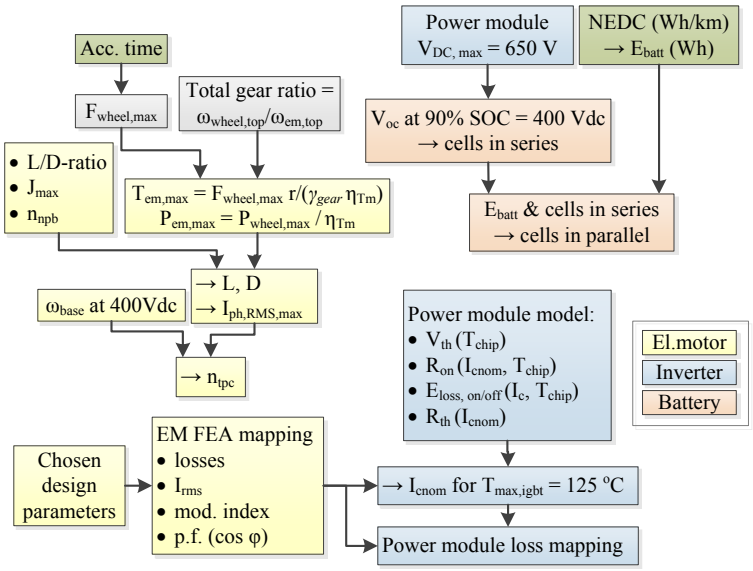

Fig. 4. BEV drive system component sizing and modelling algorithm.

III. Electric Machine Modelling, Sizing and Rescaling

A. Electric Machine Torque and Power Rating

The max speed of the motors are set to 12,000 rpm, which is in line with current BEV specifications [1]. Then the gear ratios k_{gear} are determined as the ratios of the max motor speed and the max wheel speed as in (3), and given in Table I. Furthermore, the max electric motor output torque and power are determined to be **46 kW** and **147.5 Nm** for the Small BEV, and **89 kW** and **214 Nm** for the Large. This was reached using the vehicle's max force and power requirements, wheel radius, gear ratio, and an assumed transmission efficiency of 97%.

B. Electric Machine FEA model

The reference electric motors are inset PMSMs as illustrated in Fig. 5, where the stator and rotor iron core designs are similar to that of the Toyota Prius 2004 motor with 48 stator slots and 8 poles [7]. The stator teeth and yoke are somewhat thinner than in the Prius motor and a different angle for the v-shaped magnet arrangement is used. The winding is distributed with two layers per slot and with four parallel branches. The copper fill factor in the slot area is set to 45%.

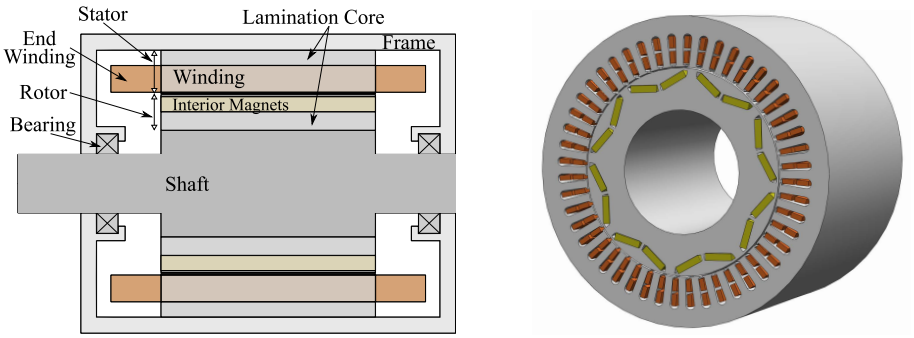

(a) Cross section. (b) Active parts.

Fig. 5. Axial cross section of machine configuration, and the active machine parts, of v-shaped reference motors.

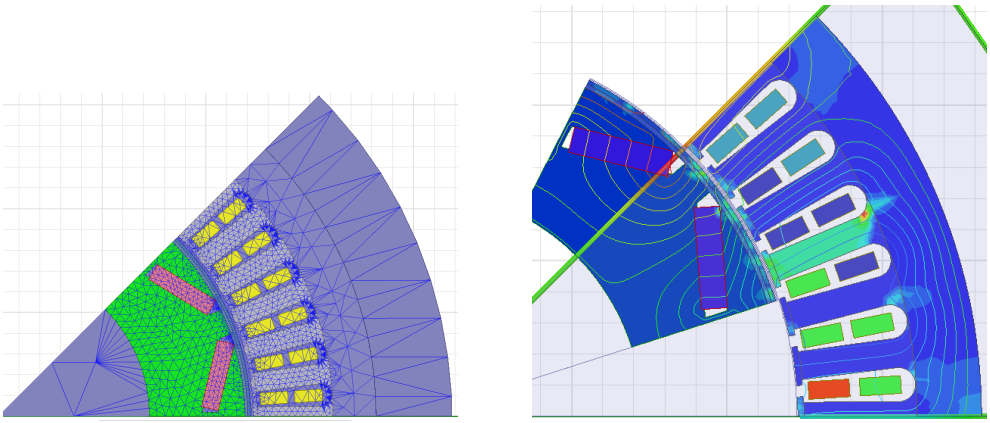

(a) Mesh. (b) Flux lines, total losses and current density.

Fig. 6. FEA of one pole of the Large motor at 4000 rpm, 251 A rms, showing mesh, vector potential flux lines, total losses in the core and magnets, as well as current density in the windings, at a certain time instant.

The Small and Large reference machine geometries are implemented and simulated in the FEA (finite element analysis) software Ansys Maxwell in 2D. The geometry and mesh density is shown in Fig. 6.

The chosen lamination material is the 0.3 mm thick NO30 by Tata Cogent [8], with a mass density of 7540 kg/m^3. Both components of the core losses (hysteresis and eddy) are calculated as mean values over the second electrical period.

A magnet with relatively low share of Dysprosium (around 3.5-4.5 w%Dy) is chosen, i.e. the Hitachi NEOMAX NMX-37F [9]. The magnet is assumed to have a working temperature of 70°C. Then the remanent flux is approximately 1.18 T, the relative permeability is 1.04, the coercivity is -902 285 A/m, the electrical conductivity is 750 469 S/m and mass density 7500 kg/m^3 [10]. In the FEA software the magnets are modeled as zero current carrying coils while considering eddy effects.

The copper conductors have a density of 8933 kg/m^3 [11], and a resistivity of $1.68\,10^{-8}$ Ωm at 20°C, with a temperature coefficient of 0.3862 $\%/K$. The windings are assumed to have a working temperature of 100°C, which is judged realistic when assuming a relatively warm coolant (65°C).

C. Electric Machine Sizing

The machine geometry is scalable both by core diameter and length. Then, in an iterative process, a suitable machine size is found for when the set max rms current density J_{max} of 20 A/mm^2, gives the desired peak torque. Simultaneously a length-to-diameter ratio (*L/D-ratio*) of 0.8 is targeted, and the number of turns per coil are adjusted in order for field weakening to start at around 3000 rpm for the Small EM and 4000 rpm for the Large, i.e. at base speed ω_{base}, for a nominal dc voltage of 400 V. These values are in line with current BEV specifications [1]. As a reference, only a few examples of L/D-ratios over one for automotive traction motors have been found, thus they seem to be rather uncommon [12]–[14].

The resulting max rms phase current is proportional to: the max rms current density; the slot fill factor k_{ff}; the slot area A_{slot}; and the number of parallel branches n_{npb}, and inversely proportional to the number of layers n_{layer} and turns per coil n_{tpc}, as in

$$I_{ph,rms,max} = \frac{J_{max}\, k_{ff} A_{slot}}{n_{layer}} \frac{n_{npb}}{n_{tpc}} \tag{4}$$

Since n_{tpc} must be adjusted to keep the voltage rating during motor length scaling, also $I_{ph,rms,max.}$ must vary.

Resulting motor parameters are shown in Table II, and mappings of the inductances and magnet flux linkage for the Large reference motor is presented in Fig 7.

TABLE II
MOTOR DATA FOR THE SMALL AND LARGE REFERENCE MOTORS.

	Small	**Large**
Max Power (at base speed, 400V_{dc})	46.0 kW	89.6 kW
Max Torque	148 Nm	215 Nm
Base speed	3000 rpm	4000 rpm
Max rms phase current	125 A	251 A
Turns per coil	10	6
Peak Efficiency (max 400 V_{dc})	96.4 %	97.1 %
Core length	136 mm	150 mm
Stator outer diameter	166 mm	182 mm
Rotor outer diameter	111 mm	121 mm
Air gap length	0.62 mm	0.68 mm
Total phase resistance (100°C)	76 mΩ	25 mΩ
d-axis inductance (L_d)	512-756 μH	219-265 μH
q-axis inductance (L_q)	1230-2042 μH	470-824 μH
magnet flux linkage (Ψ_m)	103-129 mWb	73-82 mWb

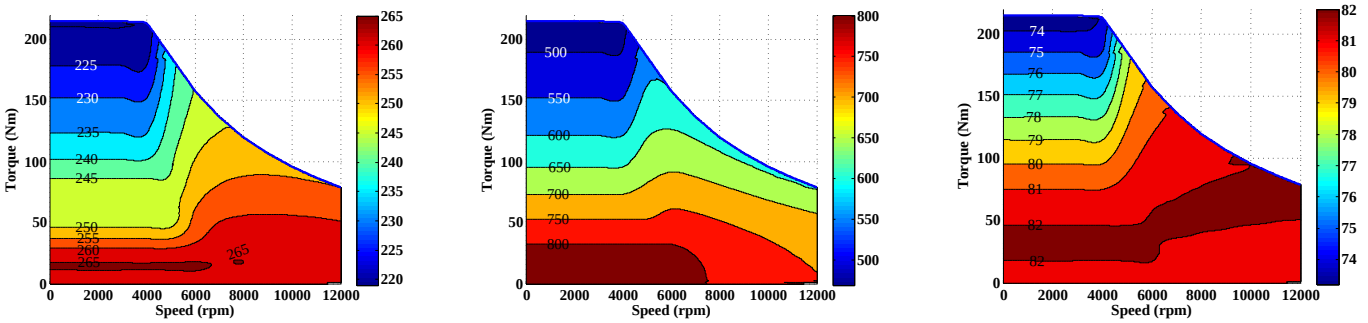

(a) L_d (μH). (b) L_q (μH). (c) Ψ_m (mWb).

Fig. 7. Inductance in the direct and quadrature axis and permanent magnet flux linkage as functions of torque and speed, for the Large reference motor.

D. Electric Machine Loss-mapping

For each machine geometry, at 13 different speed levels, 11×11 operating points in the id-iq plane have been evaluated in Maxwell, for two electrical periods with sinusoidal current excitation. The data resolution in the id-iq-plane is then increased through interpolation, from which the MTPA (Max Torque Per Ampere) operating points as well as the field weakening operation is numerically found for each integer torque level, within the allowed operating current and voltage limits. A final interpolation in the speed range is then conducted.

Due to the dynamic behaviour of the battery voltage during vehicle operation, the motor peak torque and losses are calculated at five different dc voltage levels (between 250-450V). In all cases the max rms phase current is unaltered.

When the max available dc voltage is higher, the field weakening control can start at a higher speed level. At the same time a lower field weakening current is needed in each operating point. Hence a higher max voltage leads to a higher efficiency in the field weakening region. Also the max power is linearly proportional to the change in available voltage, and changes about 25 kW per 100 V for the Large motor (or 11%-21%).

The copper losses in the active part of the winding are extracted from the FEA software. Skin and proximity effects are ignored. By estimating the length of the end winding, its share of the total winding length is used to also estimate the end winding losses.

The winding resistance is thus divided into one active part and one that represents the winding overhang. According to [15] paper D p.92, the average conductor length of a half turn, l_{av} can be expressed as

$$l_{av} = l_{active} + l_{passive} = l_{stk} + 1.2\tau_p + 2d_{ext} \tag{5}$$

where l_{stk} is the active lamination stack length, τ_p is the winding pole pitch and d_{ext} is the part of the end winding that is estimated to be axially extended outside of the lamination stack, here assumed to be 35 mm. The pole pitch is $\frac{\pi D}{2p}$, where D is the mid stator slot diameter and p is the pole pair number.

For the Large reference motor the active part is 52% of the total winding length, thus leaving 48% to the end windings.

E. Electric Machine Scaling

During production of electric machines, the iron core laminations are often stamped from core plates [16]. Since the lamination design and stamp tools are rather expensive to develop [17], electric machine manufacturers often offer different machine sizes that are based on the same stamped laminations but of different stack lengths [12], [13]. Therefore, the stack length of the reference motors are scaled linearly from 50% to 200% of the original lengths. During the length scaling the cross sectional geometry is unaltered, as is the voltage rating and the max current density. The passive end winding losses remain the same, whereas the active losses are linearly proportional to the stack length [18]. The resulting efficiencies are presented in Fig. 8. For low L/D-ratios the losses in the end windings will become more dominant. As a validation, the effect of the used linear scaling factor on mechanical output and electromagnetic losses are confirmed with additional FEA simulations. These are done at the three length scalings: 50%, 100% and 200% of the original stack length, noted as S_{min}, S_{ref}, S_{max} for the Small motor and L_{min}, L_{ref}, L_{max} for the Large.

Additionally, selected data on three scalings for both motors are presented in Table IV.

The max torque levels of the scaled motors are linearly proportional to the scaling factor. The max mass normalized wheel force for some of the scaled electric motors can be seen in Fig. 9, together with the vehicle's road load, which remains essentially the same in all cases. Even the smallest motor size will be able to sustain the vehicle's top speed requirement.

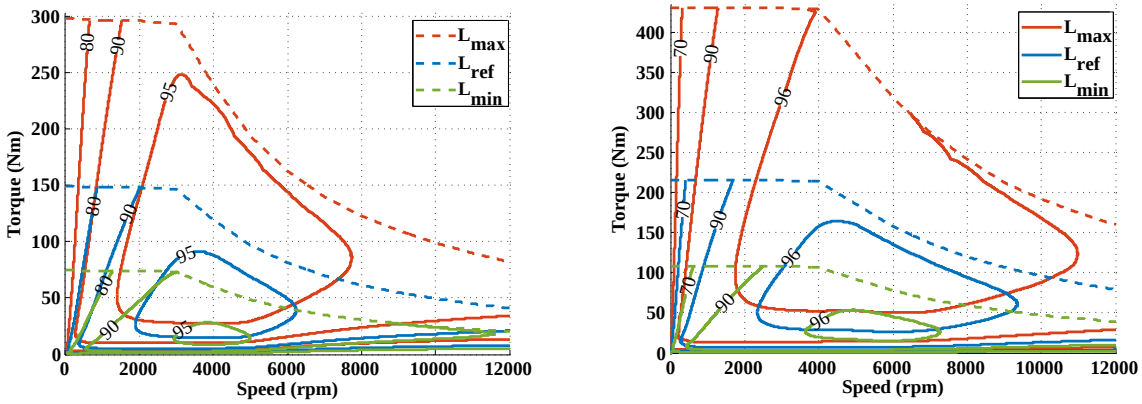

(a) Small motors. (b) Large motors.

Fig. 8. Electromagnetic efficiency contour lines (%) for three different length scalings of the Small and Large motors.

F. Mass of Machine Parts

The machine mass is estimated based on the simplified configuration shown in Fig. 5. For the active components, the mass is a product of density and volume, where volume is a product of cross sectional area and core lamination stack length. The cross sectional area of the end winding is the same as that of the active winding. The end winding length is estimated using (5) with unaltered axial extent.

The motor house is a hollow cylinder with one end cap on each side, all with a thickness of 11 mm. For simplicity, complex house textures are disregarded. It is made of die cast aluminum alloy 195 for a lightweight yet mechanically strong construction with good thermal conductivity. The mass density is 2790 kg/m^3 [19]. The density of the winding impregnation (unsaturated polyester) is 1350 kg/m^3 [15]. The shaft is made of carbon-silicon steel with the density 7817 kg/m^3 [19]. The chosen ball bearings have a mass of 190 g [20]. The mass of the different motor parts for the Small and Large BEV motors are presented in Table III.

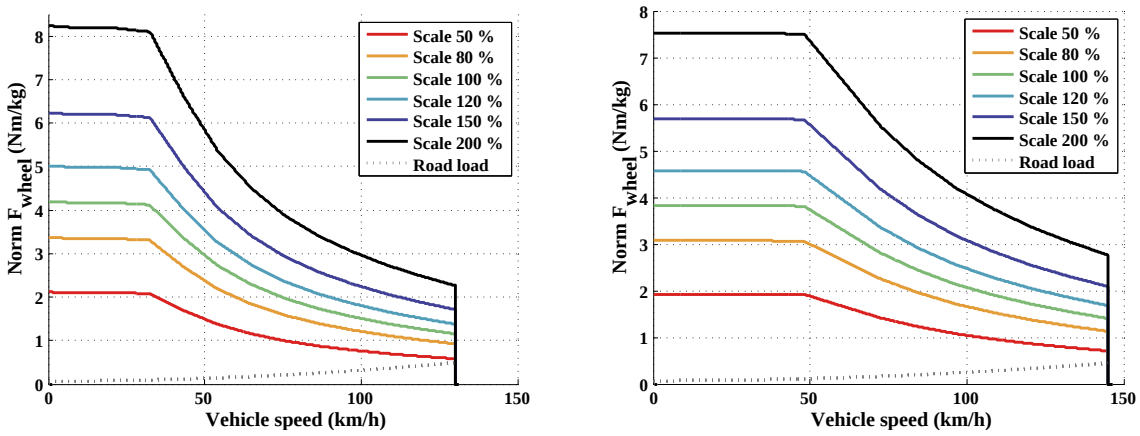

(a) Small. (b) Large.

Fig. 9. Max mass normalized wheel force as a function of vehicle speed (at 400 V DC) along with road load, for the scaled Small and Large drives.

TABLE III
MASS (KG) OF MOTOR PARTS FOR SMALL AND LARGE REFERENCE MOTORS.

	S_{ref}	L_{ref}
House	4.66	5.48
Stator Yoke	4.53	6.01
Stator Teeth	3.69	4.89
Active winding	1.83	2.42
Slot impregnation	0.34	0.45
End Winding	1.68	2.21
Magnets	0.92	1.22
Rotor laminations	5.03	6.67
Shaft	4.57	5.76
Bearings	0.38	0.38
Total Lamination	13.3	17.6
Total Copper	3.5	4.6
Total Passive Parts	11.6	14.3
Total Active Parts	16.0	21.2
Total	**27.6**	**35.5**

G. Change in Electric Machine and Vehicle Mass

The mass of the motors are estimated as the sum of the parts that scale with the stack length $m_{l_{stk}}$, and those parts that don't m_{ext}. The parts that scale with the stack length are: the stator and rotor laminations, the magnets, the active part of the winding, as well as those part of the house and shaft that are within the stack length. The scaling factor $f_{l_{stk}}$ represents the ratio of the scaled stack length and the reference stack length, i.e. it is 0.5 to 2. The mass of a scaled motor $m_{EM_{scaled}}$ is thus

$$m_{EM_{scaled}} = m_{ext} + f_{l_{stk}} m_{lstk} \tag{6}$$

The resulting mass of the scaled Small and Large motors are presented in Table IV. Even though the motor masses change from 60% to 180% of the reference motors, the effect on the vehicle mass is less than 1% for the 50% scaling factor and less than 2% for the 200% scaling factor, for both vehicles.

TABLE IV
DATA FOR MIN, REFERENCE AND MAX LENGTH SCALING OF THE SMALL AND LARGE MOTORS.

	S_{min}	S_{ref}	S_{max}	L_{min}	L_{ref}	L_{max}
L_{stk} (mm)	68	136	272	75	150	300
Turns per coil	20	10	5	12	6	3
$I_{max,rms}$ (A)	63	125	251	126	251	502
l_{active}/l_{av} (%)	34	51	67	35	52	69
m_{EM} (kg)	16.9	27.6	49.1	21.3	35.5	63.9
T_{max} (Nm)	74	148	296	107.5	215	430
$P_{max,@\omega_b}$ (kW)	23.0	46.0	92.0	44.8	89.6	179.3

IV. Inverter Power Module Modelling, Sizing and Scaling

A. A Scalable Power Module Model

A scalable inverter power module model has been constructed based on Infineon automotive 650V IGBT power modules with nominal current ratings from 50A up to 800A[1] [21]. The voltage rating of $650\,V$ is chosen, since most commercial BEVs have DC voltage levels of around $300-400\,V$ [1]. Then there is a margin for increased battery voltage e.g. when braking and for voltage peaks during IGBT turn-off.

The IGBT and diode conduction and switching losses can be modeled as in [22] where an ideal sinusoidal Pulse Width Modulated (PWM) three phase voltage is assumed. Losses dissipated in the driver and snubber circuits, as well as due to capacitive and inductive parasitics, are assumed negligible. For the IGBTs, on-state, turn-on and turn-off losses are considered, whereas the reverse blocking losses are assumed negligible. For the diodes, on-state and turn-off (reverse recovery) losses are considered, but the turn-on losses are neglected due to an assumed fast diode turn-on process.

The average on-state losses in the IGBTs and diodes in one switch can then be estimated as

$$P_{cond} = \left(\frac{1}{2\pi} \pm \frac{m_a\, cos\,\varphi}{8}\right) V_{th}\, \hat{I}_s + \left(\frac{1}{8} \pm \frac{m_a\, cos\,\varphi}{3\pi}\right) R_{on}\, \hat{I}_s{}^2 \tag{7}$$

where the plus signs adheres to IGBTs and the minus signs to diodes. The average turn-on and turn-off switching losses (per switching period) can be estimated as

$$P_{sw} = f_{sw} \cdot E_{(on+off)} \cdot \left(\frac{1}{\pi} \cdot \frac{\hat{I}_s}{I_{ref}}\right)^{K_i} \cdot \left(\frac{V_{DC}}{V_{ref}}\right)^{K_v} \tag{8}$$

The following parameters are component dependent (most are extractable from the semiconductor component data sheet)

V_{th}	on-state threshold voltage, temperature dependent
R_{on}	on-state resistance, temperature dependent
$E_{on,off}$	Energy dissipated during turn-on and turn-off
I_{ref}	Reference current, to which $E_{on,off}$ correlate
V_{ref}	Reference DC voltage, to which $E_{on,off}$ correlate (300V)
K_i	Current dependency of switching losses, (IGBT: 1, Diode: 0.6)
K_v	Voltage dependency of switching losses, (IGBT: 1.35, Diode: 0.6)

while the others are load point dependent

m_a	PWM modulation index (from EM-mapping)
φ	Phase angle between voltage and current (from EM-mapping)
$\hat{I}_s$	Amplitude of AC phase current
f_{sw}	Switching frequency (10 kHz)
V_{DC}	DC voltage level (250, 300, 350, 400, 450 V)

Due to symmetry in operation, it is enough to model the losses in a single switch, and to attribute the same power loss in the other six switches in order to find the total converter losses.

In order to make the inverter loss model scalable, the current and temperature dependence of the component specific parameters are approximated (based on the studied commercial power modules), and are presented in Table V. As can be expected, V_{th} showed little dependence on nominal collector current I_{cn} since the voltage rating is the same for all modules, whereas it decreases with increasing temperature. Both R_{on} and R_{th} show a strong current dependence and are inversely proportional to I_{cn}. Increasing chip temperature leads to increasing R_{on}. The temperature dependence of R_{th} was not covered in the data sheets, but its dependence on coolant flow rate was presented for the three top rated modules. The thermal resistance approximation used is based on the junction to coolant at 6 L/min for the FS400_H5/600/800 modules, and as the junction to heat sink for the FS50/75/200/400 modules.

The data sheet values and fitted curves are presented in Fig. 12 and Fig. 13.

Furthermore, instead of using fixed values of $E_{on,off}$ and linearly scaling them with the nominal collector current as in (8), these losses are here represented as functions of the collector current as seen in the data sheet for the top rated power module. Then the switching losses are instead calculated as

$$P_{sw,mod} = f_{sw} \cdot E_{(on,off)}(\hat{I}_s) \cdot \left(\frac{1}{\pi}\right)^{K_i} \cdot \left(\frac{V_{DC}}{V_{ref}}\right)^{K_v} \tag{9}$$

A comparison between the modules's switching losses is presented in Fig. 10, and between (9) and (8) in Fig. 11.

[1]FS50R07W1E3, FS75R07W2E3, FS200R07A1E3, FS400R07A1E3, FS400R07A1E3_H5, FS600R07A2E3 and FS800R07A2E3

TABLE V
PARAMETERS USED IN THE SCALABLE IGBT POWER MODULE MODEL.

	25 °C	**125 °C**	**150 °C**
V_{thT}	0.818 V	0.695 V	0.657 V
V_{thD}	0.956 V	0.797 V	0.733 V
R_{onT}	$688.16\,I_{cn}^{-1.002}$	$990.07\,I_{cn}^{-1.003}$	$1131.1\,I_{cn}^{-1.007}$ $(m\Omega)$
R_{onD}	$807.93\,I_{cn}^{-1.009}$	$675.61\,I_{cn}^{-1.004}$	$824.12\,I_{cn}^{-1.006}$ $(m\Omega)$
125^oC	(mJ)		
E_{onT}	$-4.1312 \cdot 10^{-6}\,I_c^2 + 0.0208\,I_c + 1.8320$		
E_{offT}	$3.9532 \cdot 10^{-8}\,I_c^3 - 3.9440 \cdot 10^{-5}\,I_c^2 + 0.0529\,I_c + 1.0603$		
E_{recD}	$-7.0598 \cdot 10^{-6} I_c^2 + 0.0187 I_c + 1.1997$		
150^oC	(mJ)		
E_{onT}	$-5.9225 \cdot 10^{-6}\,I_c^2 + 0.0230\,I_c + 1.7769$		
E_{offT}	$3.1129 \cdot 10^{-8} I_c^3 - 3.165 \cdot 10^{-5} I_c^2 + 0.0532 I_c + 1.2326$		
E_{recD}	$-9.9281 \cdot 10^{-6} I_c^2 + 0.0236 I_c + 1.3822$		
R_{thT}	$72.421\,I_{cn}^{-0.991}$ (K/W)		
R_{thD}	$80.478\,I_{cn}^{-0.954}$ (K/W)		

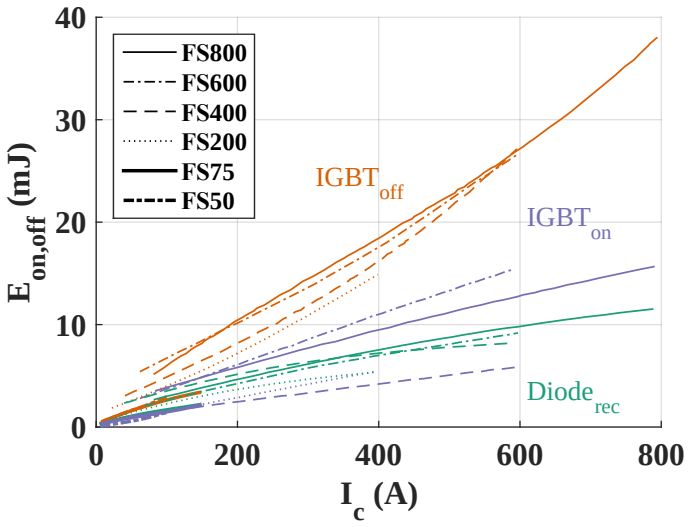

Fig. 10. Energy loss during turn on and off as a function of collector current I_c, for the commercial IGBT power modules at 125°C chip temperature, as presented in data sheets. [21]

B. Sizing and Loss Mapping of Scalable Inverter Model

The inverter module is sized such that the max IGBT chip temperature becomes 125°C in steady state. This is a matter of finding a suitable nominal collector current I_{cn} for each of the Small and Large motor inverters at the motor stack lengths, using their m_a and $cos(\varphi)$. Firstly, the operating point (torque and speed) that leads to the max chip temperature is identified using the inverter module parameters of a single module (e.g. FS800), and a coolant temperature of 65°C. During this calculation the chip temperatures are fed back to update the inverter parameters until convergence in each operating point. Secondly, the proposed scalable model presented in Table V is used, for different values of the nominal collector current, to find the current level that gives max 125°C IGBT temperature in the identified operating point. The resulting approximated relation between the max rms electric machine current and the nominal inverter current is

$$I_{cn} = 16.497 + 1.3465\, I_{rms\,max\,EM} \tag{10}$$

The inverters' nominal collector currents are presented in Table VI.

A similar method based on bare die chips is used in [23].

TABLE VI
RATED MOTOR AND INVERTER CURRENTS (I_{RMS} AND I_{CN}).

EM length	S_{min}	S_{ref}	S_{max}	L_{min}	L_{ref}	L_{max}
EM I_{rms}	63 A	125 A	251 A	186 A	354 A	692 A
Inv I_{cn}	101 A	185 A	354 A	126 A	251 A	502 A

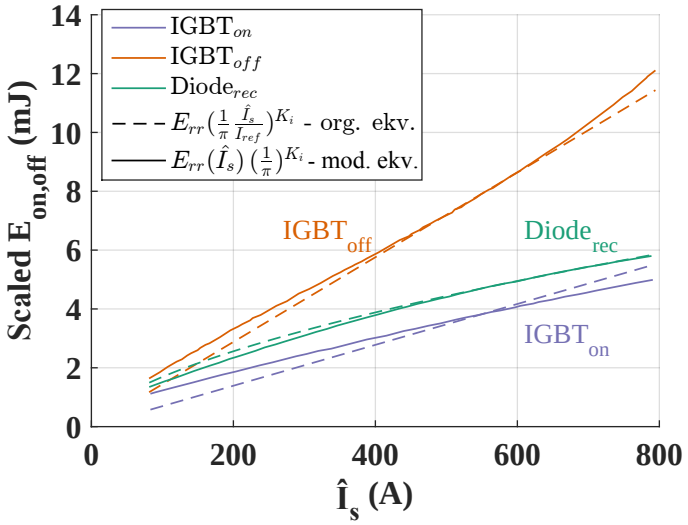

Fig. 11. Current scaling of the switching energy loss, comparing the expressions in (8) and in (9).

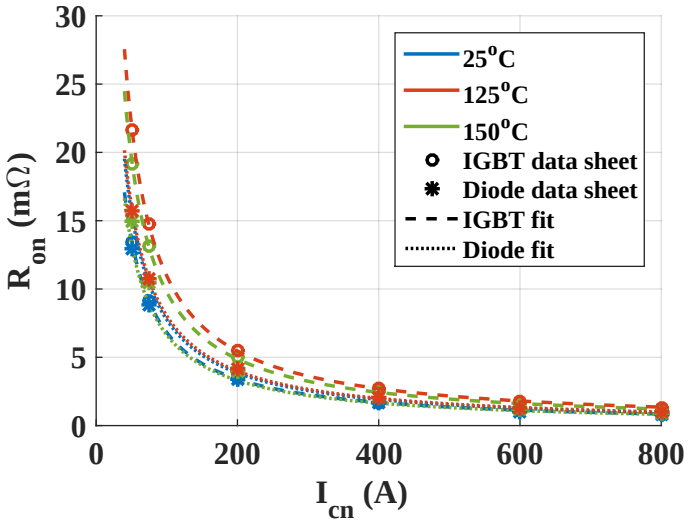

Fig. 12. On state resistance R_{on} as a function of nominal collector current I_{cnom}, for the commercial IGBT power modules, at three chip temperatures [21], as well as curve fits.

Using the suggested scalable inverter model, the losses, efficiency and steady state chip temperatures as a function of system speed and torque, for L_{ref} is presented in Fig. 14. The switching frequency is set to $10\,kHz$. At each operating point the inverter parameters are temperature adjusted in an iterative loop. The results are compared to those when using fixed chip temperatures instead (90°C for the IGBT and 75°C for the diode) in Fig. 15. When using fixed chip temperatures the losses are overestimated at low loads by up to around 10% and underestimated at higher loads by up to 7%. In terms of efficiency the differences translate to less than 1% decreased and increased efficiency. The difference is thus considered negligible. Since the computation time is also drastically reduced, the fixed chip temperatures are used when calculating the loss maps.

Finally, the inverter loss and efficiency maps are calculated for both the small and large systems at each 10% in the scaling range 50% to 200%.

For simplicity, the change in inverter mass during scaling is neglected, as it is expected to be even smaller than for the motor.

V. Battery Modelling and Sizing

A. Battery Modelling

The battery model is based on a li-ion cell of laminate type which were used in the early Nissan Leaf BEV models [24].

The charge content in the battery is expressed by the term *state-of-charge* (SOC) which changes with battery current I_b as

$$SOC(t) = SOC_{init} - \frac{\int_{t_0}^{t} I_b(\tau)\, d\tau}{Q_{tot}} \tag{11}$$

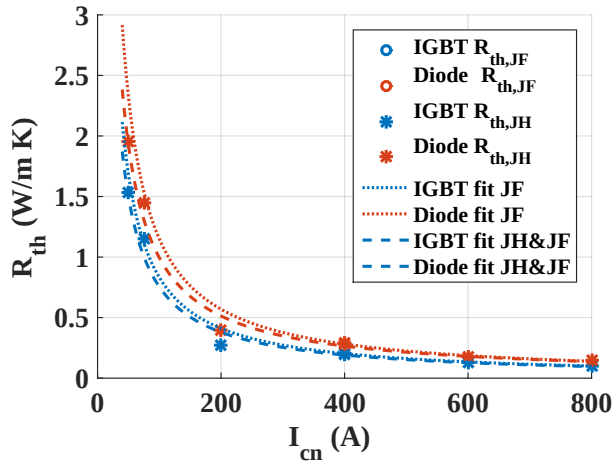

Fig. 13. Thermal resistance R_{th} as a function of nominal collector current I_{cnom}, for the commercial IGBT power modules, for the flow rate 6L/min [21], as well as curve fits.

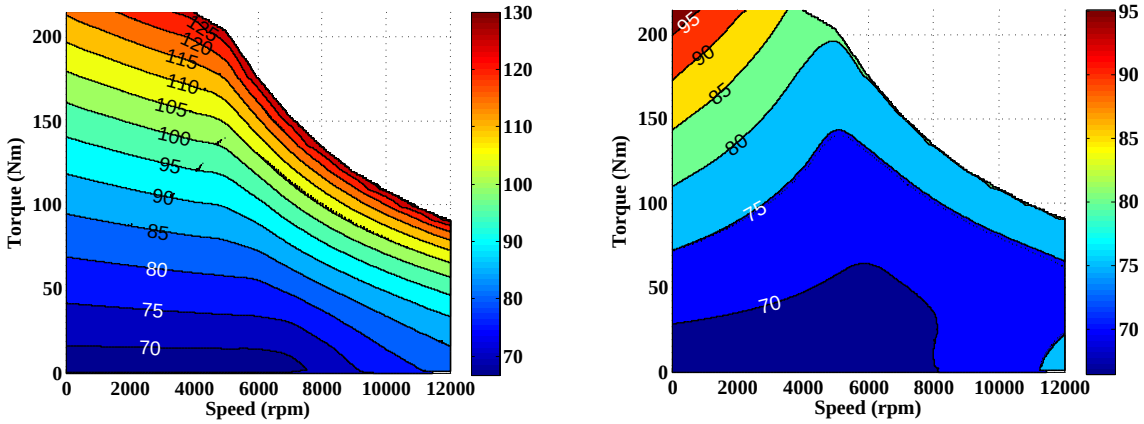

(a) IGBT temperature. (b) Diode temperature.

Fig. 14. Temperature of IGBT and diode as a function of system speed and torque, when iterating losses and chip temperature at each operating point, for L_{ref}.

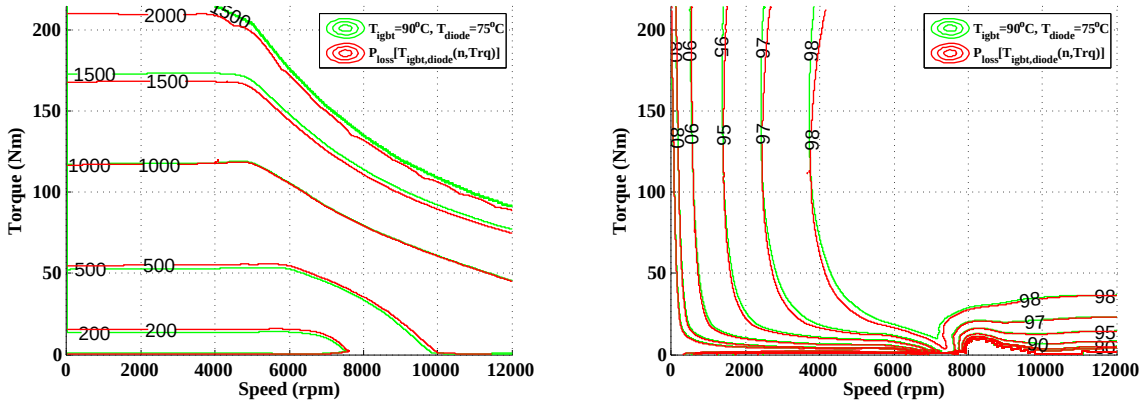

(a) Energy loss. (b) Efficiency.

Fig. 15. Total energy loss and efficiency as a function of system speed and torque, both using fixed chip temperature modelling (green) and iterative temperature and losses modelling (red), for the suggested scalable inverter model, for L_{ref}.

where SOC_{init} is the initial SOC level, Q_{tot} (Ah) is the total charge capacity of the battery.

The open source voltage as a function of state of charge (SOC) for one cell is estimated from manufacturer data [24].

The terminal voltage in the implemented battery model is the difference between the open circuit voltage and the resistive voltage drop caused by the battery current through a constant internal charging/discharging resistance R_{dis}/R_{ch}, where the

open circuit voltage varies with battery charge content [25]. The battery losses considered are thus the discharge and charging resistive (RI^2) losses.

The charge and discharge resistance are estimated based on presented measured data as a function of SOC in [26]. The used values represent an average over 10-90% SOC.

B. Battery Sizing

The number of series connected cells is chosen to be **98**, to give an open source voltage of $400\,V$ at $90\,\%$ state of charge (SOC) in both cars. The nominal battery voltage is $367.5\,V$, given a nominal cell voltage of 3.75V [24].

The number of parallel strings is found in two steps.

First the needed energy capacity according to the required NEDC driving range is estimated while assuming an average drive system efficiency of 80% and a usable SOC window of 80% (from 10 to $90\,\%$ SOC). Then, while considering an average cell charge capacity of $28.8\,Ah$ [26], the number of parallel strings is set to **2** in the Small car and **3** in the Large.

The open source voltage as a function of state of charge, along with terminal voltage during max power discharge, as well as battery discharge efficiency, are presented in Fig. 16, and the battery parameters are presented in Table VII.

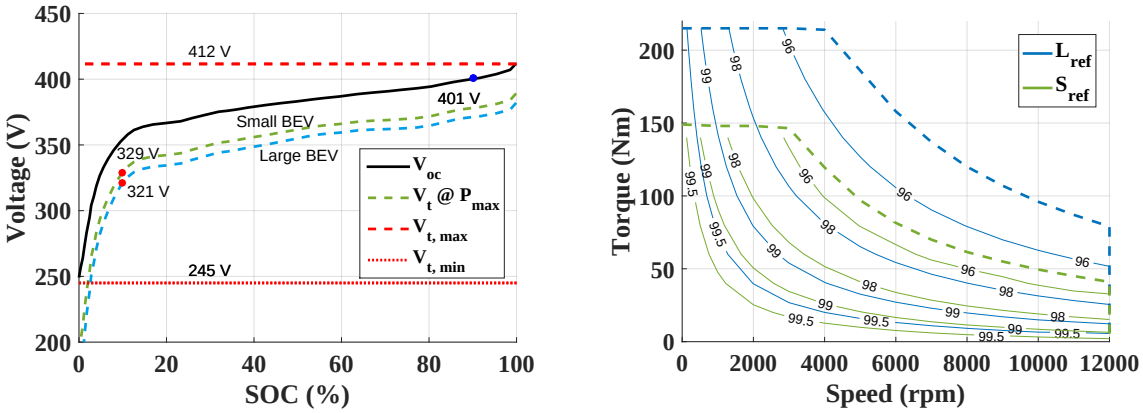

(a) Voltage. (b) Efficiency (%).

Fig. 16. Battery model open source voltage as a function of SOC, along with terminal voltage during max power discharges, as well as battery discharge efficiency in the motor operating area, for the Small and Large BEVs.

TABLE VII
BATTERY MODEL PARAMETERS FOR SMALL AND LARGE BEVS.

	Small BEV	**Large BEV**
Total energy:	21.2 kWh	31.8 kWh
Series connected cells:	98	98
Parallel strings:	2	3
R_{dis}	141 $m\Omega$	94 $m\Omega$
R_{ch}	118 $m\Omega$	79 $m\Omega$

VI. TRANSMISSION MODELLING

Automotive transmission efficiency depends on the gear ratio, the current operating speed and torque as well as the fluid temperature, where the efficiency decreases with increasing speed, while it increases with increasing torque as well as by fluid temperature [27], [28].

Analytical generic loss modelling of transmissions however, are rare as torque independent loss models must be empirically or experimentally based [29]. Therefore their general validity is strongly limited.

In this work, it is desired to include speed and torque dependent transmission losses in order to investigate the general behavior and effect for various driving patterns. Therefore, a generic torque loss model presented by [28], has been implemented. The torque loss is modeled as a polynomial with six scalar coefficients, five of which are combined with the input torque and speed both linearly and squarely, as well as the product of the two inputs. Suitable numerical ranges for the coefficients, representing light truck multi speed manual transmissions of various manufacturers are also presented in [28]. This model was also used in [30], where it is a bit further described.

The resulting transmission efficiency as function of input torque and speed can be seen in Figure 17 for S_{ref}.

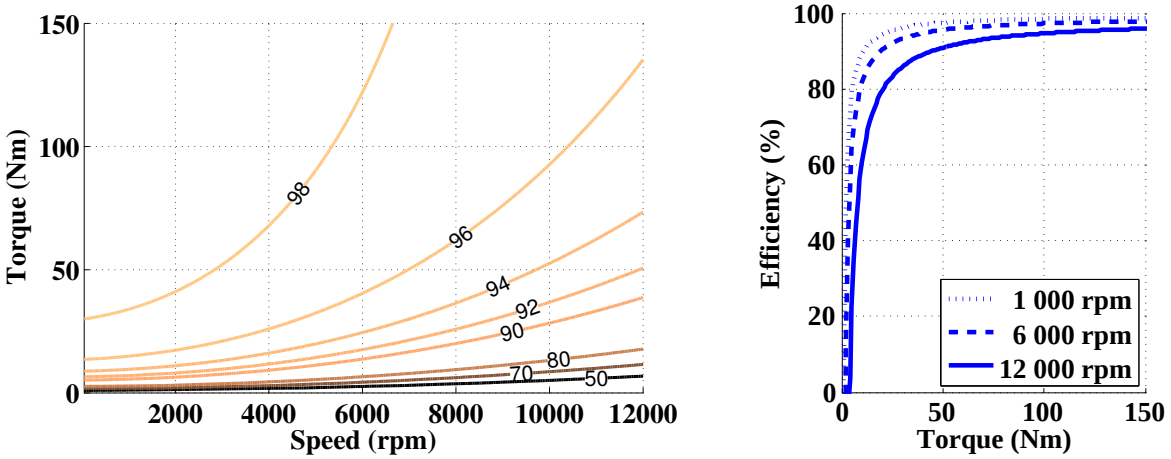

(a) Efficiency (%).

(b) Efficiency (%).

Fig. 17. Transmission model efficiency as a function of system torque and speed.

VII. Conclusions

In this report the electric drive system of a Small and a Large BEV are sized based on vehicle performance requirements. The electromagnetic motor losses are determined via finite element analysis (FEA) and inverter losses by algebraic expressions. The motor and inverter models are complemented with load dependent battery and transmission loss models.

Scalable models regarding mechanical output, losses, and mass for two differently sized representative BEV electric machines have been derived and the sizing consequence on the efficiency has been determined.

Based on the Infineon FS power module series, a scalable inverter loss model has been derived. Using data sheet information of chip losses and thermal properties, and setting the max operating chip temperature to 125^oC, a dimensioning relation has been established between the inverter current rating and the max rms phase current.

The operating temperatures of the diode and transistor chips have been determined in the torque-speed map, showing higher transistor temperatures than diode temperatures. In addition, the consequence of using a constant mean temperature in the power electronic chips when determining the efficiency has also been established, showing that using a mean temperature works very well (10% underestimation at high loads and 7% overestimation at low loads).

Acknowledgment

The financial support through Chalmers Area of Advance Transport (AoAT) is gratefully appreciated.

References

[1] E. A. Grunditz and T. Thiringer, "Performance analysis of current bevs based on a comprehensive review of specifications," *IEEE Transactions on Transportation Electrification*, vol. 2, no. 3, pp. 270–289, Sept 2016.

[2] R. Sehab, B. Barbedette, and M. Chauvin, "Electric vehicle drivetrain: Sizing and validation using general and particular mission profiles," in *Mechatronics (ICM), 2011 IEEE International Conference on*, April 2011, pp. 77–83.

[3] F. Le Berr, A. Abdelli, and R. Benlamine, "Sensitivity study on the design methodology of an electric vehicle," in *SAE 2012 World Congress & Exhibition*. SAE International, apr 2012. [Online]. Available: https://doi.org/10.4271/2012-01-0820

[4] S. W. Moore, K. M. Rahman, and M. Ehsani, "Effect on vehicle performance of extending the constant power region of electric drive motors," in *SAE Technical Paper*. SAE International, 03 1999. [Online]. Available: http://dx.doi.org/10.4271/1999-01-1152

[5] M. Ehsani, Y. Gao, and A. Emadi, *Modern Electric, Hybrid Electric, and Fuel Cell Vehicles: Fundamentals, Theory, and Design*, 2nd ed. CRC Press, Taylor & Francis Group., 2010.

[6] K. Rajashekara, "Present status and future trends in electric vehicle propulsion technologies," *IEEE Journal of Emerging and Selected Topics in Power Electronics*, vol. 1, no. 1, pp. 3–10, March 2013.

[7] J. S. H. et. al. (2005) Report on toyota prius motor thermal management. Oak Ridge National Laboratory. Accessed 2013-06-29. [Online]. Available: http://info.ornl.gov/sites/publications/Files/Pub57487.pdf

[8] (2015) Hi-lite no30 data sheet. Cogent. Accessed 2015-05-19. [Online]. Available: http://cogent-power.com/cms-data/downloads/Hi-Lite_NO30.pdf

[9] (2014) Hitachi review vol. 63, no. 3, p.113. Hitachi Metals, Ltd. Accessed 2015-05-28. [Online]. Available: http://www.hitachi.com/rev/specialissue/2014/ebook/index.html#page=1

[10] (2015) Neodymium-iron-boron magnets neomax, home page. Hitachi Metals, Ltd. Accessed 2015-05-27. [Online]. Available: http://www.hitachi-metals.co.jp/e/products/auto/el/p03_21.html

[11] F. Incropera, D. Dewitt, T. Bergman, and A. Lavine, *Fundamentals of Heat and Mass Transfer*. John Wiley & Sons, 2007.

[12] M. Lenz. (2011) Individual e-mobility system solutions for automotive and off-highway applications. Boscg Engineering GmbH. Presentation, Accessed 2015-06-30. [Online]. Available: http://www.a3ps.at/site/sites/default/files/conferences/2011_eco-mobility2011/2011_Eco-Mobility_01_03_Lenz.pdf

[13] (2010) Remy hvh250 series electric motors, specifications. Remy Electric Motors, Remy International Inc. Accessed 2016-09-01. [Online]. Available: https://www.remyinc.com/docs/HVH250_r3_Sept_2010.pdf

[14] T. A. B. et. al. (2011) Evaluation of the 2010 toyota prius hybrid synergy drive system. Oak Ridge National Laboratory. Accessed 2013-11-27. [Online]. Available: http://info.ornl.gov/sites/publications/files/Pub26762.pdf

[15] J. Lindström, "Development of an experimental permanent-magnet motor drive," Licentiate of Engineering, Technical Report No. 312L, Chalmers University of Technology, apr 1999.

[16] J. Hendershot and T. Miller, *Design of Brushless Permanent-Magnet Machines*. Motor Design Books LLC, 2010.

[17] G. Lanza, J. Stoll, and A. Krmer, "Assessment of lamination stack production," in *Electric Drives Production Conference (EDPC), 2013 3rd International*, Oct 2013, pp. 1–8.

[18] S. Stipetic, D. Zarko, and M. Popescu, "Ultra-fast axial and radial scaling of synchronous permanent magnet machines," *IET Electric Power Applications*, vol. 10, no. 7, pp. 658–666, 2016.

[19] Y. A. Çengel, *Introduction to Thermodynamics and Heat Transfer*. Mcgraw-Hill, 2008.

[20] (2016) Ball bearings. SKF. Accessed 2016-03-30. [Online]. Available: http://www.skf.com/group/products/bearings-units-housings/ball-bearings/index.html

[21] (2017) Automotive igbt modules 650v. Infineon Technologies AG. Accessed 2017-01-27. [Online]. Available: http://www.infineon.com/cms/en/product/power/igbt/automotive-igbts/automotive-igbt-module/channel.html?channel=db3a30432ba3fa6f012be33e87b75915#goto_producttable

[22] A. Wintrich, U. Nicolai, W. Tursky, and T. Reimann. (2011) Application manual power semiconductors. Semikron International GmbH. [Online]. Available: https://www.semikron.com/dl/service-support/downloads/download/semikron-application-manual-power-semiconductors-english-en-2015

[23] G. Domingues-Olavarria, P. Fyhr, A. Reinap, M. Andersson, and M. Alakula, "From chip to converter: a complete cost model for power electronics converters," *IEEE Transactions on Power Electronics*, vol. PP, no. 99, pp. 1–1, 2017.

[24] (2014, jan) Aesc home page. AESC, Automotive Energy Supply Corporation. Accessed 2014-03-14. [Online]. Available: http://www.eco-aesc-lb.com/en/product/liion_ev/

[25] L. Guzzella and A. Sciarretta, *Vehicle Propulsion Systems - Introduction to Modeling and Optimization*, 2nd ed. Springer, 2007.

[26] (2011) 2011 nissan leaf - vin 0356. Idaho National Laboratory (INL), Advanced Vehicle Testing Activity (AVTA). Accessed 2014-02-04. [Online]. Available: http://avt.inel.gov/pdf/fsev/batteryleaf0356.pdf

[27] M. A. Kluger, J. J. Greenbaum, and D. R. Mairet, "Proposed efficiency guidelines for manual transmissions for the year 2000," in *SAE Technical Paper*. SAE International, 02 1995. [Online]. Available: http://dx.doi.org/10.4271/950892

[28] J. J. Greenbaum, M. A. Kluger, and B. E. Westmoreland, "Manual transmission efficiency trends and characteristics," in *SAE Technical Paper*. SAE International, 11 1994. [Online]. Available: http://dx.doi.org/10.4271/942274

[29] M. Mägi, "On efficiencies of mechanical coplanar shaft power transmissions," Thesis for the degree of Doctor of Philosophy, Chalmers University of Technology, 1974.

[30] E. A. Grunditz and T. Thiringer, "Characterizing bev powertrain energy consumption, efficiency, and range during official and drive cycles from gothenburg, sweden," *IEEE Transactions on Vehicular Technology*, vol. 65, no. 6, pp. 3964–3980, June 2016.